SAND2011-9369C

Flash X-Ray Measurements of Shock Wave Interactions with Dense Particle Fields

Justin L. Wagner,[1] Steven J. Beresh,[2] Sean P. Kearney,[3] Brian O. Pruett,[4] Elton K. Wright[5], and Gerald C. Stoker[6]
Sandia National Laboratories, Albuquerque, NM, 87185

A flash x-ray imaging system has been used to make volume fraction measurements during the interaction of a Mach 1.66 planar shock wave with a dense gas-solid field of particles. The particle field was generated by a gravity-fed method that resulted in a spanwise parallel curtain of 100-micron particles having a volume fraction of about 20%. During the first 280 microseconds of the interaction, the peak volume fraction decreased from about 22% to about 5%. With increasing time, the field propagated downstream and spread in an asymmetric fashion with a steeper gradient in volume fraction on the downstream side of the field compared to the upstream side. Bias errors associated with geometric distortion were identified and techniques to minimize them were discussed. X-ray velocimetry methods were evaluated using sample tracer particle images. X-ray particle image velocimetry was shown to be feasible for particle fields having a thin spanwise dimension, but is expected to fail for spanwise thick particle fields. To make measurements in a curtain of substantial spanwise thickness, a one-component, volumetric x-ray PTV technique is suggested.

Nomenclature

A	=	x-ray mass attenuation coefficient
I	=	x-ray intensity
I_0	=	initial x-ray intensity
IOD	=	image to object distance
M	=	Mach number
P	=	static pressure
SOD	=	x-ray source to object distance
S	=	spot size width
b	=	spot size blur width
t	=	time
w	=	width through which x-rays travel
w_0	=	spanwise width of particle curtain
x	=	streamwise coordinate
y	=	wall-normal coordinate
z	=	spanwise coordinate
Δ	=	displacement

[1] Senior Member of the Technical Staff, Engineering Sciences Center, P.O. Box 5800, Mailstop 0825; jwagner@sandia.gov. AIAA Member.
[2] Principal Member of the Technical Staff, AIAA Associate Fellow.
[3] Principal Member of the Technical Staff, Engineering Sciences Center, AIAA Associate Fellow.
[4] Senior Technologist, Engineering Sciences Center.
[5] Principal Technologist, Geothermal Center.
[6] Augmented Staff Member, Engineering Sciences Center.

This work is supported by Sandia National Laboratories and the United States Department of Energy. Sandia National Laboratories is a multi-program laboratory managed and operated by Sandia Corporation, a wholly owned subsidiary of Lockheed Martin Corporation, for the U.S. Department of Energy's National Nuclear Security Administration under contract DE-AC04-94AL85000.

Δ_{SO} = source to object distance in x-ray particle image velocimetry measurements
Δ_{IO} = image to object distance in x-ray particle image velocimetry measurements
θ = angle between the center of the particle field and source centerline
ρ = density
σ = standard deviation
φ_p = particle volume fraction

Subscripts
g = glass
i = interaction
rms = root-mean-square
s = shock

I. Introduction

THE explosive dispersal of particles occurs in a variety of engineering problems, including in heterogeneous detonations, where solid particles are initially mixed with explosive material [1]. During early charge expansion, the particles are densely-packed within the expanding gas and the resulting particle dynamics highly influence the continuing reaction. Although understanding the dense particle transport within the expanding gas is crucial to develop dependable physical modeling, the underlying phenomena that occur in dense gas-solid flows is currently very limited. A dense gas solid flow has a particle volume fraction φ_p of about 0.1-50%. In contrary to dilute ($\varphi_p < 0.1\%$) and granular flows ($\varphi_p > 50\%$), there has been very little research [2, 3] focused on dense gas solid flows, where φ_p resides between about 0.1-50% [1].

To fill the knowledge gap for shock-particle interactions with initial volume fractions residing between the dilute and granular limits, a multiphase shock tube (MST) was recently constructed [4, 5]. The facility uses a gravity-fed seeding method to generate a dense, spatially isotropic field of 100 micron diameter particles into which a planar shock is driven. Previous work [4, 6-7] used sensors to measure the unsteady pressures during the interaction at various locations upstream and downstream of the initial particle field location. In addition, high-speed schlieren imaging was used to capture the wave structure associated with the interaction such as shocks, expansions, and to provide a measure of particle dispersion. Although these data provided insight into the flow and particle behavior in the dense gas-solid regime, it was not possible to penetrate the optically dense particle field with visible light.

Several studies have used x-ray sources to make quantitative measurements in flows opaque to visible light. For example, synchrotron radiation sources have been utilized to make volume fraction measurements of droplet sprays [8], as well as particle velocimetry measurements in liquid flows [9, 10]. To perform measurements at the MST, a commercially available solution is desired. Seeger et al. [11] used a continuous wave medical system to make velocimetry measurements in a liquid volume column. However, for the current study, a continuous system would not provide adequate light in the microsecond timescales of interest. Alternatively, flash x-ray sources are able to provide intense beams that last tens of nanoseconds, essentially 'freezing' the flow in a similar fashion to laser diagnostic measurements in fluids experiments. For example, Meekunnasombat et al. [12] utilized a 150 kV flash x-ray system to measure the volume fraction of a shock-accelerated water layer.

The current experiments also use a flash x-ray imaging system to demonstrate two important capabilities 1) particle volume fraction measurements, and 2) x-ray particle velocimetry measurements. The first task is accomplished by measuring the x-ray attenuation through the particle field, which allows the particle volume fraction to be calculated. Results are presented showing the evolution of the particle volume fraction during about 300 microseconds of a $M_s = 1.66$ interaction. The velocimetry capability is then demonstrated from tests that used two x-ray sources. Images of a stationary target containing tin tracer particles are used to evaluate the feasibility for making x-ray particle image velocimetry (x-ray PIV) and particle tracking velocimetry (x-ray PTV) in future shock tube tests.

II. Experimental Method

A. The Multiphase Shock Tube

A schematic of the multiphase shock tube (MST) used to study the interaction of shock waves with dense fields of particles is shown in Fig. 1. A high-pressure compressed nitrogen system provides the driver gas. The driver section is a 2.1 m long stainless steel pipe with an inner diameter of 88.9 mm and a wall thickness of 12.7 mm. Cruciform scored, nickel alloy burst disks (BS&B Safety Systems) are used as the diaphragms that initially separate

the driver gas from the driven gas. According to the manufacturer, burst pressures are repeatable to 5%, which results in a jitter in burst time of about 4 seconds [4]. Burst disks with nominal burst pressures of 1100 kPa, 2760 kPa, and 4140 kPa are used to produce shock Mach numbers of about 1.66 ± 0.02, 1.92 ± 0.02, and 2.02 ± 0.02, respectively.

As shown in Fig. 1, the 5.2 m long driven portion consists of sections made from extruded square aluminum tubing having a nominal wall thickness of 12.7 mm. Although there is an abrupt change from a circular to square cross section, pressure measurements have shown that the shock is well planar by the time it the test section [4]. The driven sections are cut from one piece of extruded aluminum tubing having a nominal inner width of 76.2 mm and are assembled in a modular fashion. Since the inner width of the extruded square tubing was measured to vary by about 1 mm, the inner walls of the last five sections were machined to a width of 79.2 ± 0.2 mm to minimize steps upon assembly of the sections. The driven gas is air at an initial temperature of about 296 K and an initial atmospheric pressure of about 84.1 kPa. Table 1 gives a summary of the experimental conditions for the three possible nominal shock Mach numbers. The modular design of the driven section allows for the location of the test section to be interchangeable. In Fig. 1 the second to last driven section has been replaced by what is termed the 'particle curtain' test section, which also has inner width of 79.2 mm.

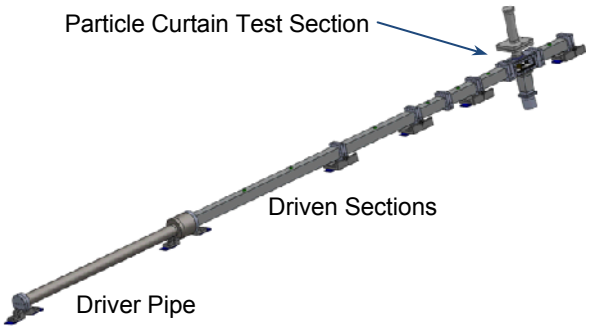

Fig. 1 Schematic of the multiphase shock tube [4].

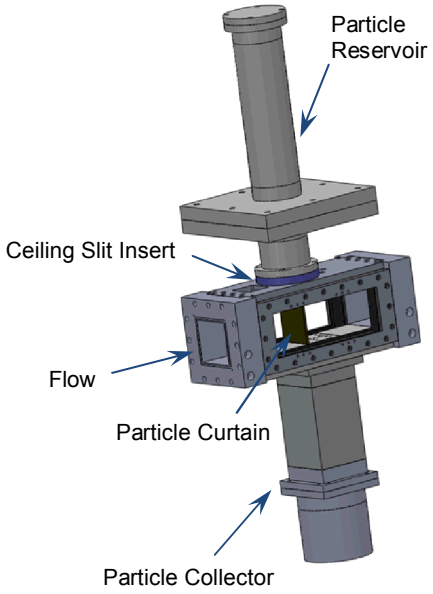

Fig. 2 Particle curtain test section [4]: Schematic of the apparatus used to shape the gravity-fed particle flow into a locally spatially isotropic curtain.

The unique aspect of this shock tube is its ability to provide multiphase flows within the dense gas-solid regime by implementing a gravity fed particle curtain, or particle 'rain,' as shown in Fig. 2. An aluminum reservoir is used to initially store spherical soda lime particles that are sieved to diameters of 100-126 μm. Prior to an experiment, the soda lime particles rest on an initially closed industrial gate valve. During a test, but prior to the rupture of the burst disk, the gate valve opens and the particles flow through a beveled slit in the ceiling insert reaching a nearly constant flow rate in about 100 ms. The particles exit the test section through a similar slit in the floor and then enter a particle collector reservoir. The slit has a width w_0 of about 87% of the full span of the test section, with a streamwise thickness 3.2 mm. The gravity-fed seeding apparatus shapes the particles into what is termed the particle curtain, which narrows to a streamwise thickness h of about 2 mm for the bottom 75% of the test section height.

A photo of the curtain acquired at an oblique angle with a test section wall removed is shown in Fig. 3. The photo suggests that the curtain is locally isotropic. The particle volume fraction of the curtain was calculated by measuring the mass flow rate of particles through the ceiling slit and imaging the curtain to determine the velocity of the falling particles [4]. There is some variation in particle volume fraction with curtain height since it is gravity driven. The volume fraction at the center of the curtain is 19 ± 2%. Owing to gravity, the volume fraction of the curtain varies approximately linearly from about 24 ± 2% at the ceiling to about 13 ± 2% at the floor. The particles flow at a velocity of about 1 m/s, which makes them essentially frozen compared to the shock velocities. Further details concerning the characterization of the shock tube, and the generation of the particle curtain are given in Ref. 4.

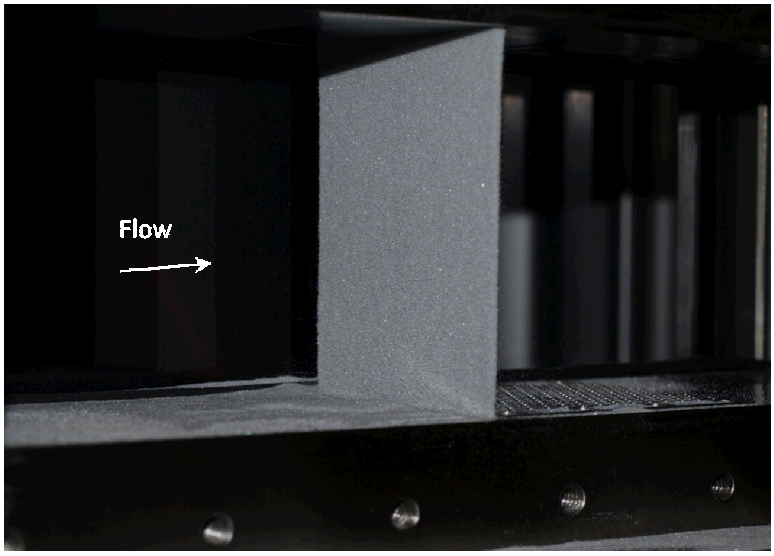

Fig. 3 Photo of the particle curtain [4].

Table 1: Shock Tube Experimental Conditions

M_s	P_4, kPa	P_1, kPa	T_4, K	T_1, K	W_s, m/s
1.66 ± 0.02	1242 ± 45	82.7 ± 1.6	298 ± 2	296.4 ± 1	568 ± 15
1.92 ± 0.02	2935 ± 170	82.7 ± 1.6	299 ± 2	296.4 ± 1	671 ± 13
2.02 ± 0.02	4170 ± 350	82.7 ± 1.6	297 ± 1	296.4 ± 1	696 ± 08

B. Flash X-Ray System

A photo of the 450 kV flash x-ray system is given in Fig. 4. The system has two channels of output, each having a characteristic photon energy of 450 keV, which corresponds to a wavelength of about 3 pm. Owing to bremsstrahlung (brems) radiation, the x-ray energy has a broad distribution with the peak in the its energy spectrum occurring at about one-third the electron energy, or at about 150 keV (9 pm).

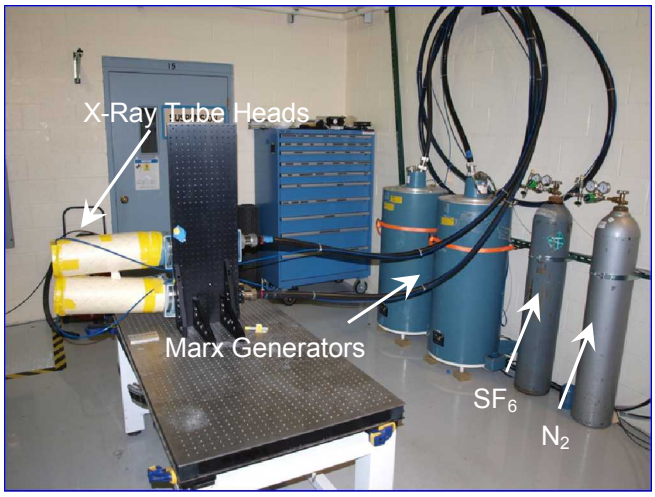

Fig. 4 Photo of the 450 kV flash x-ray system.

The system operation is as follows. Prior to firing a channel of the system, a Hewlett Packard Marx generator (model 43734-62900) is charged to a potential of 27-35 kV, (depending on the desired photon flux), with a L-3 communications high-voltage power supply (model 3147A). Sulfur hexafluoride and nitrogen are used in the system for dielectric purposes. Upon triggering, about 6 kA of current flows from the capacitor banks to the x-ray tube heads that contain tungsten anodes, resulting in an intense x-ray beam having a duration of about 25 nanoseconds. It takes about 10 seconds to charge each Marx generator, so only once shot of each channel per shock tube test is possible. At a distance of about 1m from the point source output, the energy in each incident beam is at a maximum about 20 mR.

Several options exist for the x-ray tubes. Tubes with an effective spot size S of 1-5 mm are readily available from L-3 Communications. The benefit of using a larger spot size is increased tube life, while the benefit of using a smaller spot size as is discussed below is improved image quality. With the latter benefit in mind, the tube heads used for the current work had an effective spot size of about 1 mm. The tube head life was found to be about 50 shots.

A Rad-icon detector (RadEye2 EV) was used to image the incident x-rays. The sensor used a Gadolinium Oxide scintillator to convert x-ray photons to visible photons that were imaged by a CMOS sensor. The 12-bit sensor had 1k × 1k array of 100 micron pixels. Owing to readout limitations, the minimum delay between the triggering of the detector and image recording was about 150 ms. Since it takes roughly 10 ms for the incident shock to travel down the length of the shock tube, a shock could not be used to trigger the detector.

The experimental timing sequence was therefore as follows. The detector was instructed to begin recording during the pressurization of the driver section. Although a shock wave could not be used to begin recording, it could be used to end recording, which resulted in detector integration times of about 2-4 seconds. It was desirable to minimize the sensor integration time to minimize detector noise. A ceiling sensor (PCB 113B27) at x_i = -68.6 mm was used to trigger the flash x-ray source. At M_s = 1.66, it takes the incident shock about 120 μs to reach the upstream edge of the curtain at x_i = 0. Using the x_i = -68.6 mm pressure signal, and a Stanford Research Systems delay generator (DG645), the particle field was imaged at interaction times t_i = 0-280 μs, where t_i = 0 corresponds to the impingement of the shock on the curtain. A delayed signal from the x_i = -68.6 mm sensor was also used to trigger the detector to end recording. Details of the fast-response pressure measurement system are given in Ref. 2.

C. Image Processing

A standard flat-field correction process was applied to each test image. Prior to the acquisition of each image, an offset image was acquired without x-ray signal to account for variations in background intensity of the CMOS sensor. The offset varied from about 100-400 counts. To correct for variations in detector response to the x-rays, as well as true variations in the x-ray beam, a full-scale, or gain image was also acquired. The gain image was corrected by subtracting the offset image. Following an offset subtraction, the test images were then normalized by the corrected gain image resulting in a near flat-field image where particles were not present. An example of such an image showing the particle field at an interaction time of t_i = 280 μs is given in Fig. 5a. The image is 100 mm × 64 mm^2 and is located at the wall-normal center of the test section.

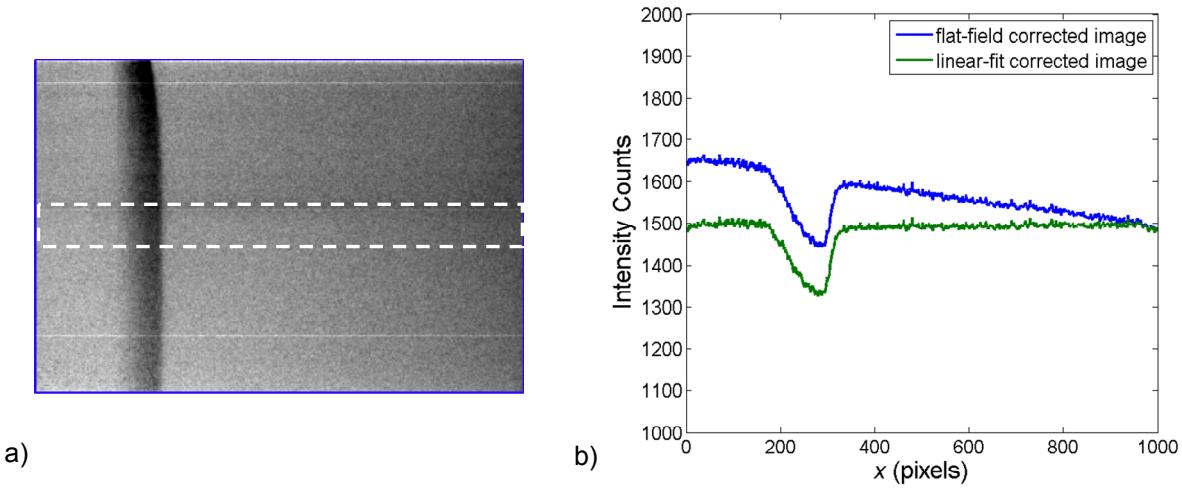

Fig. 5 Particle field at t_i = 280 μs: a) image (100 × 64 mm^2) following a standard flat-field correction procedure showing the 8mm tall rectangle over which the streamwise intensities are averaged, and b) averaged streamwise intensity profile for the image and a linear-fit corrected profile.

The streamwise intensity profile averaged over the middle 8 mm of the image in Fig. 5a is shown in Fig. 5b. Even with the flat-field correction described above there is a clear nearly linear decrease in intensity with increasing streamwise position in locations where no particles are present (about 0-150, and 400-1000 pixels). This artifact is attributed to noise acquired during the four second integration time of the image. Although not repeatable, each image acquired in the study exhibited a nearly linear pattern of changing intensity across the streamwise dimension of the image. Therefore, on an image-by-image basis, an additional correction using a linear fit was performed. As is demonstrated below, for all images presented, this additional correction successfully brought the intensity levels to a nearly constant value for pixels outside of the particle field location.

Finally, all images shown in this paper have been contrast adjusted to best show their relevant features.

III. Particle Volume Fraction Measurements

A. Experimental Setup and Calibration

A schematic of the setup used to measure the particle volume fraction during an interaction is shown in Fig. 6. The schematic is in the plan-view (x-z) plane. Each sidewall of the test section was outfitted with an aluminum window having a length of 225 mm, a height of 64 mm, and a thickness of 10 mm. One x-ray source that was vertically (y-axis) aligned with the test section wall normal center was used. The x-ray source to object (SOD) distance was 136 cm, where the object location is defined here to be at the spanwise center of the test section, or at z = 0. The detector was attached to the test section sidewall at a distance (IOD) of about 8 cm from z = 0. The x-ray beam originates from a point source with a finite spot size S, which results in a spot size blur b [13]:

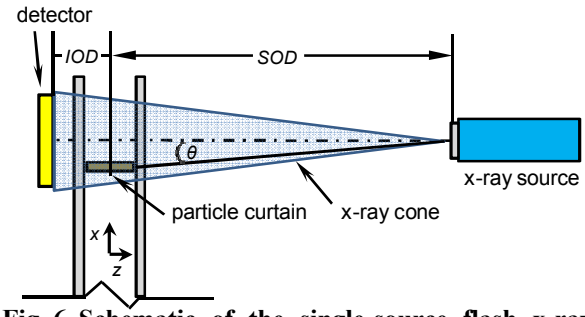

Fig. 6 Schematic of the single-source flash x-ray configuration used to measure the particle volume fraction during an interaction with a spanwise parallel curtain.

$$b = \frac{S \times IOD}{SOD} \tag{1}$$

Since the particles span 87% percent of the test section width, their blur will vary with spanwise location. With the experimental geometry of Fig. 6, the blur width for particles at the detector side of the test section (z = -4 cm) is about 30 microns. The blur increases to about 90 microns for particles at the source side of the test section (z = 4 cm).

The typical image field-of-view presented herein is given in Fig. 7. The image size was about 50 × 64 mm^2, which covered 500 × 640 pixels^2 of the detector. The initial curtain location was in the upstream portion of the image to allow for recording during the downstream propagation of the particle field. As is shown in Fig. 6, this resulted in an angle between the streamwise center of the curtain and the centerline of the x-ray source θ of about 1-degree. As will be discussed, this small angle influences the measurement bias errors.

The Beer-Lambert law predicts than an incident x-ray beam with incident intensity I_0 traveling through a medium with density ρ and thickness w, will be attenuated to intensity I [14]:

$$I/I_0 = e^{-A\rho w} \tag{2}$$

where A is the mass x-ray attenuation coefficient (having units of cm^2/g), which has been tabulated [14] for common materials as a function of incident intensity I_0 and wavelength. Thus if the mass attenuation coefficient, incident beam properties, and material properties of the medium are known, the total thickness of the medium can be computed. Since our flash x-ray source has a broad spectrum, a calibration method was utilized to determine the mass x-ray attenuation coefficient A.

The mass x-ray attenuation coefficient A is a function of the incident wavelength. Rather than account for the broad photon energy distribution of the beam and the attenuation through the aluminum test section windows, a calibration method with a glass step-wedge was employed. During the calibration, the step-wedge was placed in the test section with the test section walls in place. The step-wedge consisted of fifteen glass microscope slides that were each 75 mm × 25.4 mm × 0.96 mm. The density of the glass slides was 2.4 g/cm^3. The slides were stacked such that incident x-rays passed through fifteen steps of increasing glass thickness. The step-wedge appears in the bottom of the image shown in Fig. 8a. At the left of the image, the x-rays have passed through 15 glass slides. From left to right, for about every 40 pixels, the thickness decreases by 0.96 mm resulting in the sixteen different intensity levels. Note that the right of the image corresponds to an area without the step wedge where the x-rays were attenuated only by the aluminum windows. This area defines I_0 for the calibration.

The intensity in the image of Fig. 8a was averaged over the 25.4 mm height of the wedge resulting in the stepped plot of Fig. 8b.

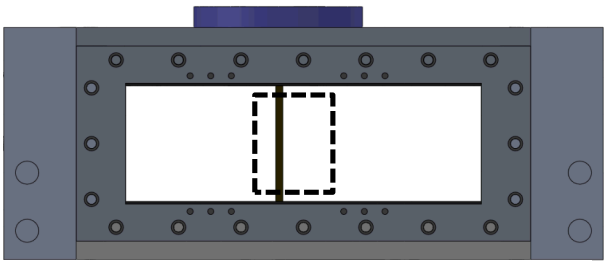

Fig. 7 X-ray imaging field-of-view for the particle concentration measurements.

The intensity of each step was then averaged over its length in x of about 40 pixels producing the measured attenuation curve of Fig. 9. The range in intensities is nearly identical to that measured during interaction tests with glass spheres. By least squares regression, the measured data were fit to Eq. (2) to solve for the mass x-ray attenuation coefficient using two fit techniques: 1) using a constant A, and 2) using a piecewise fit with A that varied for each of the fifteen glass steps. The constant fit yielded A = 0.124 cm^2/g. Owing to brems radiation, the peak in the intensity spectrum should occur at about 150 keV. According to the National Institute of Standards [14], at a photon energy of 150 keV, the attenuation coefficient through Pyrex glass is 0.139 cm^2/g, which is within a reasonable 12% of the current measurement. As shown in Fig. 9, the piecewise fit better matches the calibration data. For the piecewise fit A varies from about 0.135 for the highest intensities, to about 0.116 at the lowest intensities. It is expected that the piecewise fit should give more accurate results since the attenuation through the glass spheres should be similar to that through the step wedge. This was found to be the case, as is discussed below.

A goal of the current work is to determine the particle volume fraction of the particle field following the impingement of the incident shock. Assuming a constant particle curtain spanwise width w_0, the volume fraction of the curtain through a given cross section is given by:

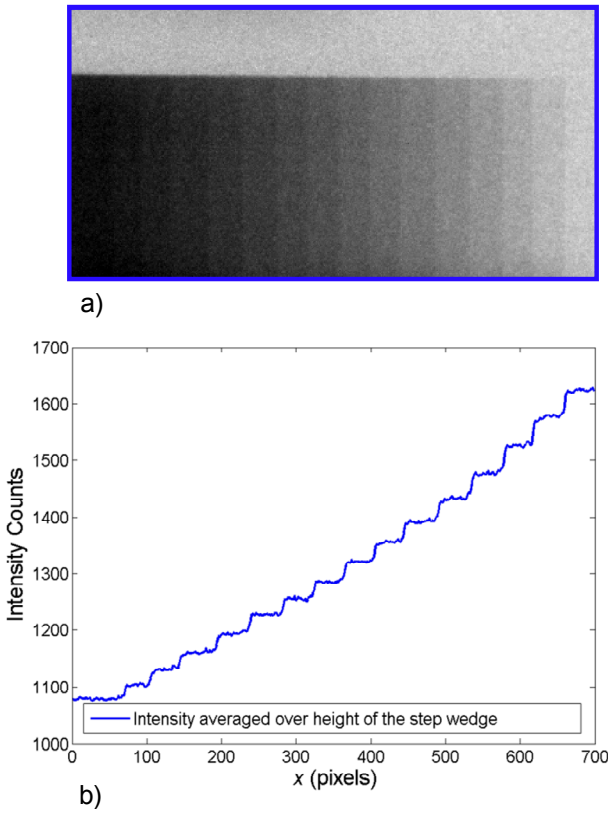

Fig. 8 Glass step-wedge: a) image, and b) intensity averaged over the height of the step wedge.

$$\varphi = {w_g}/{w_0} \tag{3}$$

where w_g is the total width of soda lime spheres through which the x-rays have traveled. Substituting w_g given from Eq. (3) into Eq. (2) and solving for φ yields:

$$\varphi = \frac{\ln\frac{I}{I_0}}{-Aw_0\rho_g} \tag{4}$$

where ρ_g is the density of the soda lime glass, which is 2.52 g/cm^3.

The particle volume fraction of the particle field is then calculated with Eq. (4) and two assumptions: 1) The soda lime spheres result in the same x-ray attenuation as the glass step-wedge, and 2) The thickness of the particle field remains constant with w_0 = 68.6 mm. To test the former assumption, a calibration with a step-wedge consisting of soda lime spheres can be used in future calibrations.

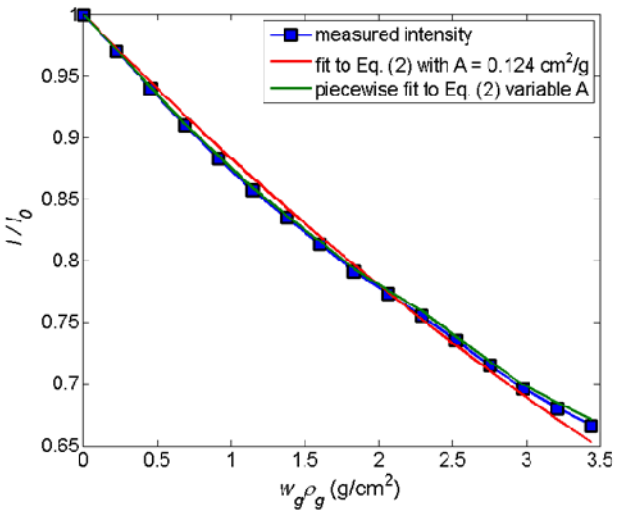

Fig. 9 Step-wedge intensity measurements and least-squares regression fits to Eq. (2)

B. Particle Volume Fraction during an Interaction

Since only one flash x-ray image can be acquired per interaction experiment, images from different interactions are pieced together to form a pseudo-sequence. This method is justified by the fact that fast-response pressure measurements and high-speed schlieren imaging have shown the interaction to be

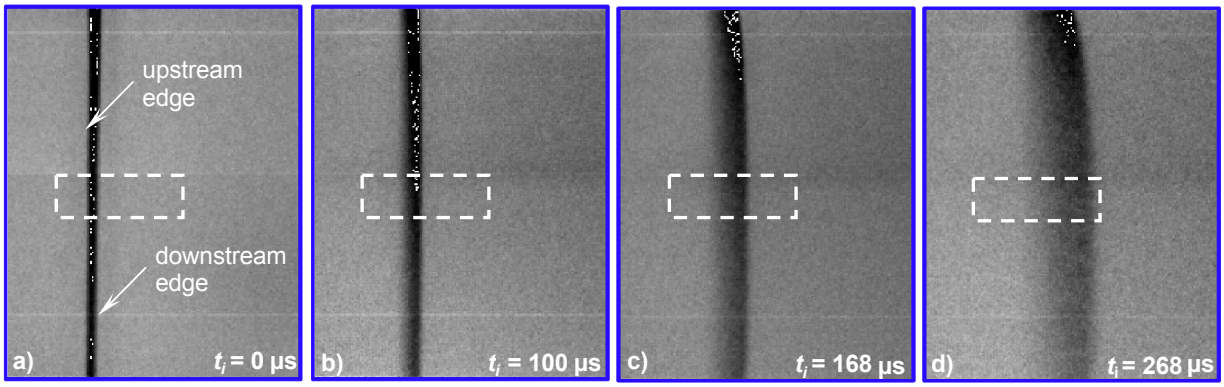

Fig. 10 Flash x-ray images showing the evolution of the particle field during M_s = 1.66 interactions at times: a) t_i = 0 µs, b) t_i = 110 µs, c) t_i = 180 µs, and d) t_i = 280 µs. The white rectangle shows the location used to produce the volume fraction profiles given in Fig. 11.

repeatable. A pseudo-sequence of images acquired during three different M_s = 1.66 interactions is presented in Fig. 10. The image fields-of-view are 50 × 64 mm^2 and their location in the test section is given Fig. 7.

The image in Fig. 10a corresponds to an undisturbed particle curtain prior to the arrival of the incident shock. From the image, an average streamwise intensity profile was produced as described in the imaging processing section above. The rectangular annotation in Fig. 10a shows the location for the profile. The volume fraction profile of the undisturbed curtain, which was calculated using the streamwise intensity profile and Eq. (4) is shown in Fig. 11 (t_i = 0 µs). Note that for all results, a variable A_c was used according to the piecewise fit shown in Fig. 9. As is discussed below, the variable A_c fit gave more physically plausible results. The peak volume fraction is about 22%,

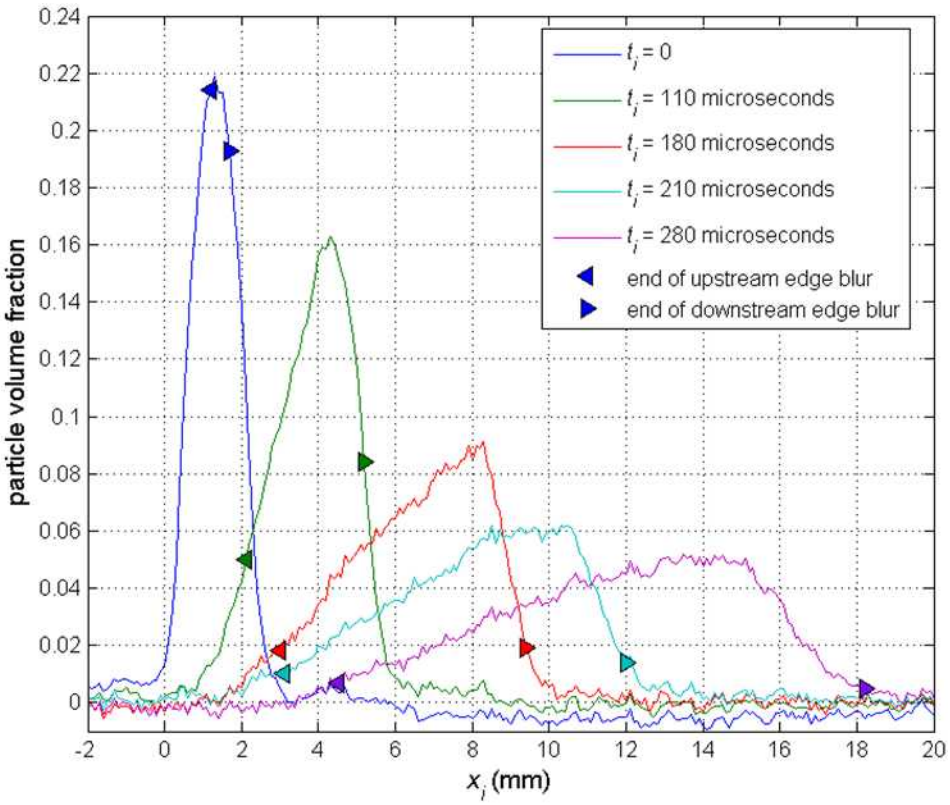

Fig. 11 Volume fraction profiles at five different interaction times using the averaged streamwise profiles in the areas denoted in Fig. 10 and Eq. (5).

which is in good agreement with previous measurements that used imaging of the curtain and a precision scale [4] to give a volume fraction of 19 ± 2%.

It is expected that the true volume fraction distribution is closer to a top-hat profile than the profile in Fig. 9 suggests. Two factors contribute to the apparent broadening of the displayed profile. The first is the blur caused by the finite spot size S (Eq. 1), which is expected to broaden the apparent curtain width by a total of about 0.2 mm. The second contributor, as is illustrated in Fig. 6, is the 'geometric distortion' that occurs as the diverging x-rays travel through the span of the test section. As is discussed in the appendix, from the geometry of experimental setup, the distances for which the volume fraction profiles appear blurred have been estimated for both the upstream and downstream sides of the profiles. The estimated locations where the blur ceases to influence the volume fraction profiles (i.e., the 'end of edge blur' markers) are plotted for each profile. For example, the $t_i = 0$ profile is affected by geometric distortion from about 0 to 1.2 mm on the upstream side of the curtain and from about 1.7 mm to 3 mm on the downstream side of the curtain. Therefore, nearly the entire profile of the undisturbed curtain has been geometrically distorted. As is discussed in the appendix, to minimize the blur, it is necessary to minimize the angle between the center of the measurement location and the centerline of the source θ (in Fig. 6). Note that if this angle were zero, the geometric distortion would only be about 0.2 mm, instead of the roughly 2 mm shown in Fig. 11. Although the geometric distortion affects the upstream and downstream sides of the profiles, useful observations can be made in the regions for which the profiles are not expected to be blurred (i.e, the profile portions inside the 'end of blur markers').

As is shown in Fig. 9, following the arrival of the incident shock at the curtain and with continuing time, the particle field propagates downstream while spreading. A previous study provided details on the wave structure associated with the interaction and the resulting particle dispersal [4]. Although the previous schlieren imaging was able to capture useful observations, it was not able to quantify the volume fraction of the field during an interaction, owing to the opacity of the particle field towards visible light. Conversely, the current images show a varying intensity through the particle field.

The intensity profiles from each image were used to calculate the five volume fraction profiles that are displayed in Fig. 10. The profiles were calculated using the image pseudo-sequence of Fig. 9 and Eq. (5). Again, note that valid observations can be made for the profile portions that fall within the 'end of blur' markers. The distribution of the streamwise volume fraction can be seen as it evolves with interaction time, providing unprecedented details of the particle field that otherwise would be hidden within its opacity. From t_i = 0-280 μs, the width of the particle field grows as it moves downstream and the peak volume fraction decreases from about 22% to about 5%. With increasing time, the field spreads in an asymmetric fashion having a steeper gradient in volume fraction on the downstream side of the field. For example, at t_i = 180 microseconds the upstream side of the profile (from x_i = 3 – 8.3 mm) has a volume fraction gradient of about 0.014 / mm, while the downstream side (from x_i = 8.3 – 9.4 mm) has a volume fraction gradient with nearly five times the magnitude at about -0.066 / mm.

Conservation of mass implies that the integration of each volume fraction profile should yield the same result. A summary of profile integrals is shown in Table 2 for profiles generated using the piecewise fit method that used a variable A_c and for profiles (not shown here) obtained using a constant A_c = 0.124. The 95% confidence intervals show a variation of about 24% for the profiles generated with the piecewise calibration, compared to about 31% for those that used a constant A_c. Since the piecewise fit seemed to give more physically correct results it was used for the profiles in Fig. 11.

Table 2: Integrals of volume fraction profiles (normalized to average)

t_i	Integral (variable A_c)	Integral (A_c = 0.124)
0	0.88	0.82
110	1.07	1.03
180	0.99	1.01
210	0.96	1.00
280	1.09	1.13
95% confidence interval	± 0.24	± 0.31

Previous measurements [4] indicated that the total particle mass in a given curtain varies by about 11%. Therefore, agreement between the profile integrals should not be expected to be less than 11%. The current 24% variation in profile integrals does however indicate that there is room for improvement. Although it is difficult to draw conclusions based on the five profiles, it is likely that several factors contributed to an increased measurement

error. These include calibration error, detector noise, and bias errors associated with geometric distortion. Future experiments will work to understand better these measurement uncertainties.

Developing the capability to measure the particle volume fraction during an interaction accomplishes the first goal for the flash x-ray diagnostics. Having such diagnostics at hand augments further the unique capabilities of the MST to provide high-fidelity data for shock wave interactions with dense particle fields. These measurements quantitatively reveal particle dynamics of the spreading particle field that would not be discernable by conventional measurement techniques using visible light.

IV. X-Ray Particle Image Velocimetry Demonstration

A. Experimental Setup

To evaluate the feasibility for making x-ray particle image velocimetry measurements during a shock tube test two flash x-ray channels were used, as is shown in Fig. 12. Note that the schematic is in the end-view (y-z) plane. Owing to the detector readout time, velocimetry measurements during a shock tube test require a double-exposure of the x-ray sources. In order to illuminate the same portion of the test section, the total angle between the sources θ_2 was about 10-degrees. In future tests with a particle curtain, tracer particles will be mixed with the glass beads that form the curtain. In order to obtain tracer contrast, they must attenuate more than the surrounding glass beads. A good candidate for such a tracer is tin.

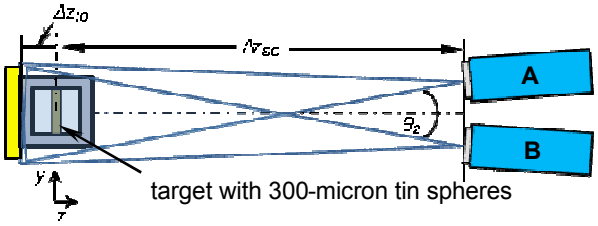

Fig. 12 Schematic of the dual-source configuration used for x-ray velocimetry measurements of a streamwise parallel particle field

The current work used a test target consisting of 300-micron, tin spheres adhered to a 5 mm thick acrylic sheet. As shown in Fig. 12, the sheet was aligned parallel to the streamwise dimension and placed near the spanwise center of the test section (z = 0). The source to object (target) distance along the spanwise coordinate Δz_{SO} was about 100 cm. The image (detector) to object distance along the spanwise coordinate Δz_{IO} was about 8.4 cm.

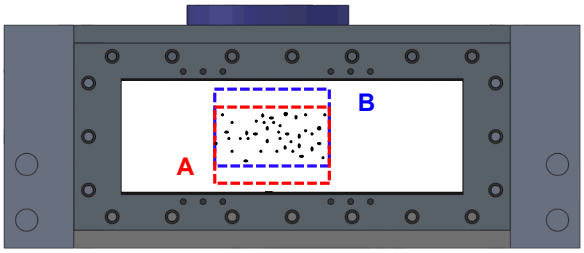

Fig. 13 Field-of-view for the x-ray particle imaging velocimetry evaluation.

The field-of-view for the tracer imaging is given in Fig. 13. Since the sources were angled with respect to z-axis, the image from each source appeared on the detector at a different y-location. The lower rectangle represents the location of the image from the upper x-ray source (A) and the upper rectangle denotes the image from the lower source (B). The area where the rectangles overlap corresponds to the PIV field-of-view. From geometry, a stationary, double-exposed object will appear in the image plane at two different y-locations at a spacing of:

$$\Delta y' = 2\Delta z_{IO} \tan\frac{\theta_2}{2} \tag{5}$$

Equation (5) and the experimental configuration predict that a stationary, double-exposed object should appear with a spacing of about 14.7 mm, corresponding to 147 pixels.

B. Sample Results

Sample images of the stationary target containing the 300-micron tin spheres tracer particles are shown in Fig. 14. The tin spheres are observed as the dark spots in the images. The useful areas image areas correspond to locations without occlusion from test section hardware and are shown with rectangular annotations that are consistent with those in Fig. 13. Again, the image from each source will appear shifted in the y-direction and the apparent spacing between images of a particle should be given according to Eq. (5). With the current setup it is necessary to acquire a double-exposed image on the detector for a shock tube experiment with the particle curtain. To replicate such a double-exposure, the image in Fig. 14a was superimposed onto the image of Fig. 14b, resulting in the image of Fig. 14c.

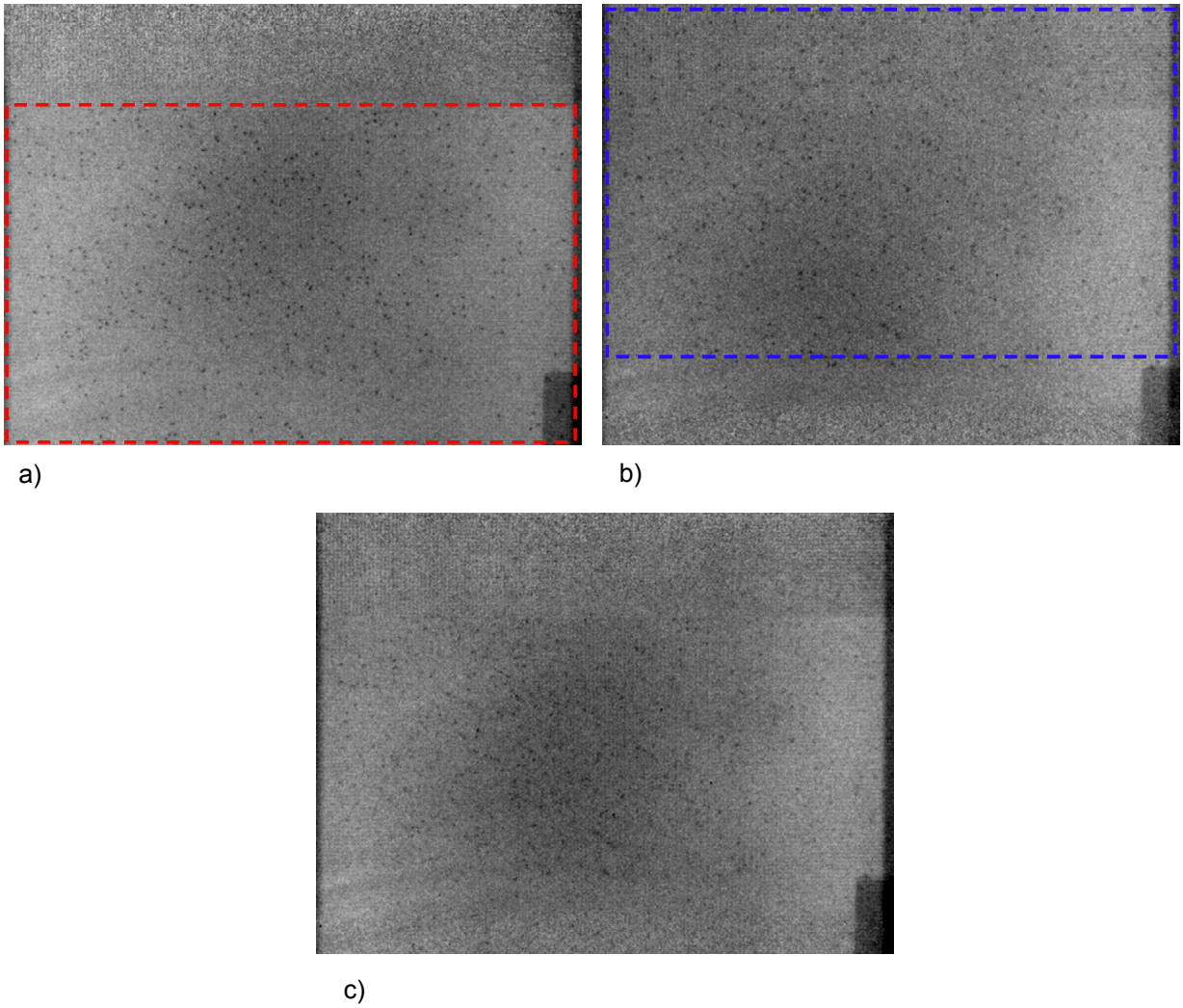

Fig. 14 Flash x-ray images of the target containing 300-micron tin spheres: a) image from tube head A, b) image from tube head B, and c) addition of Fig. 14a and Fig. 14b.

The images in Fig. 14a and Fig. 14b were used to compute vector fields using the cross-correlation algorithm implemented in the software package LaVision Davis 8.2. An autocorrelation algorithm was applied to the image in Fig. 14c. An initial window shift with a displacement of Δy = 150 pixels (15 mm) was applied to the first pass to account for the geometrical shift. The images were interrogated with an initial pass using 64 × 64 pixels^2 (6.4 × 6.4 mm^2) interrogation windows, followed by three iterations of 32 × 32 pixels^2 (3.2 × 3.2 mm^2) interrogation windows, with a 50% overlap. The resulting vector fields were validated based upon a signal-to-noise ratio with a requirement that $Q_{12} > 1.05$ and a nearest-neighbor 3× 3 median filter, where vectors having a displacement component with a deviation outside the range of $\pm 2\sigma$ were removed.

The vector field from the cross-correlation of Fig. 14a and Fig. 14b is shown in Fig. 15a. The amount of valid vectors is about 50%. For a standard PIV application, this percentage would be considered low. However, for the novel application of the current flash x-ray system to an optically opaque medium, this result is encouraging. The average x displacement Δx is about -1.7 pixels, with a standard deviation Δx_{rms} of about 1.2 pixels. The average y displacement is about 150 pixels, with a standard deviation Δy_{rms} of about 1.2 pixels. The measured Δy is near that approximated by Eq. (5) and the measured Δx is about 0 as it should be for the stationary target. The vector field from the autocorrelation of Fig. 14c is given in Fig. 15b. The amount of valid vectors is about 20% lower than its cross-correlation counterpart. The average Δy and Δx are about 148 and 0.5 pixels, respectively. Owing to the noisier image, the standard deviations Δy_{rms} and Δx_{rms} are about three times greater than those for the cross-correlated vectors. Although there is certainly room for improvement, it seems plausible that the current setup would work to measure velocities in an optically opaque field during a shock tube test.

Although, the tests with the sample target suggest that x-ray PIV measurements can performed for a curtain that has a thin spanwise dimension, there is a substantial limitation for the current x-ray PIV setup. The images have Δy shifts that are dependent on the spanwise location z. In tests with a curtain that has a large spanwise thickness, the tracer particles will exist at many z locations. Integrating throughout the entire test volume will therefore result in many Δy shifts. With each interrogation window having many Δy displacements, PIV algorithms will fail. Fortunately, PTV algorithms would not be subject to the same problems.

The geometry of the current experimental setup could be advantageous to particle tracking velocimetry (PTV) measurements. Since PTV tracks individual particles, a vector would be given for each particle. High-speed schlieren imaging at the edges of the particle field [4] suggest that the particle flow is predominantly one-dimensional. If one assumes one-dimensional flow particle flow, then the apparent Δy from PTV measurements could be used to determine the z location of a particle. This would result in a one-component volumetric measurement of velocity through the entire test section width.

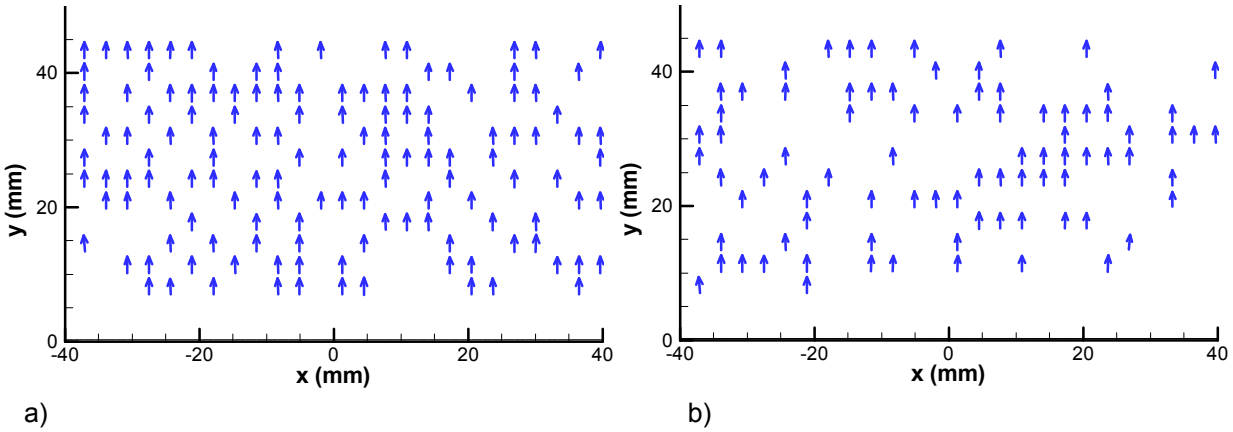

Fig. 15 X-ray PIV vector fields: a) cross-correlated field using the images of Fig. 14a and Fig. 14b, and b) vector field from the autocorrelation of Fig. 14c.

V. Conclusions and Future Work

Flash x-ray measurements have been made in experiments involving the interaction of a M_s = 1.66 shock wave with a dense field of particles. The particle field that consisted of 100-micron glass spheres, had a streamwise thickness of about 2 mm, a volume fraction of about 20%, and it was aligned parallel to the spanwise direction of the test section.

Images during an interaction were used to produce streamwise volume fraction profiles using the Beer-Lambert law and measured mass x-ray attenuation coefficients. The coefficients were determined with a calibration technique that used a glass step wedge. It was found that using a piecewise varying attenuation coefficient produced more physically correct results than a constant coefficient.

The evolution of the streamwise volume fraction distribution was shown for interaction times of 0 through 280 microseconds. The peak volume fraction in the curtain was measured to initially be about 22%, which is in good agreement with previous measurements that used an alternative method. Following the impingement of the incident shock, the particle field propagated downstream with the peak volume fraction decreasing to about 5% at 280 microseconds. The particle propagation occurred in an asymmetric fashion, with the downstream side of field experiencing a greater volume fraction gradient than the upstream side.

The geometry of the experimental setup was analyzed to estimate the geometric distortion associated with the diverging point source x-rays and angular misalignment of the source and measurement volume. Although bias errors were identified in the current data, they do not alter the conclusions stated above. However, in order to obtain high fidelity volume fraction measurements, particularly at early interaction times, it is necessary to minimize the geometric distortion. Future measurements will do so by minimizing the angle between the source centerline and the particle field centerline.

Two flash x-ray sources and a single detector were utilized to evaluate the potential to make x-ray particle velocimetry measurements. Owing to the response time of the detector, a double-exposure is required. Images were acquired of a stationary target containing 300-micron tin spheres. It was found that x-ray PIV measurements should be possible in shock tube tests, but only for curtain geometries that have thin spanwise widths. To make

measurements in a curtain of substantial spanwise thickness, a one-component, volumetric x-ray PTV technique was proposed.

VI. Appendix: Evaluation of Geometric Distortion

A. Comparison of X-ray Measurements to Schlieren Imaging

To assess potential bias errors, the x-ray data are compared to that given from previous schlieren imaging [4, 7]. The upstream and downstream edges of the particle field are defined using the volume fraction profiles in Fig. 11. For each of the profiles, the upstream edge is defined to be the location where the volume fraction has increased to 5% of the peak value. Similarly, the downstream edge is defined to be the location where the volume fraction has decreased to a value of 5% of the peak. The edges given from the x-ray data are compared to those obtained from previous schlieren imaging. In the schlieren imaging experiments, the light source was collimated and care was taken to ensure that the collimated beam was normal to the test section. The particles appeared in shadow resulting in zero intensity within the particle field. The schlieren upstream edge position was defined to occur when the intensity decreased to 5% of that in the particle-free background. Similarly, the downstream edge position was defined to coincide with the location where the intensity increased to 5% of the background.

The edge positions from both methods are displayed in Fig. 16a. The schlieren plots in Fig. 16a were averaged from four Mach 1.66 interaction experiments and their corresponding uncertainty bars are 95% confidence intervals based on the data scatter. The upstream edge positions given by both methods are in good agreement, but the downstream edge positions for the x-ray data are several mm higher greater than those given with the schlieren technique.

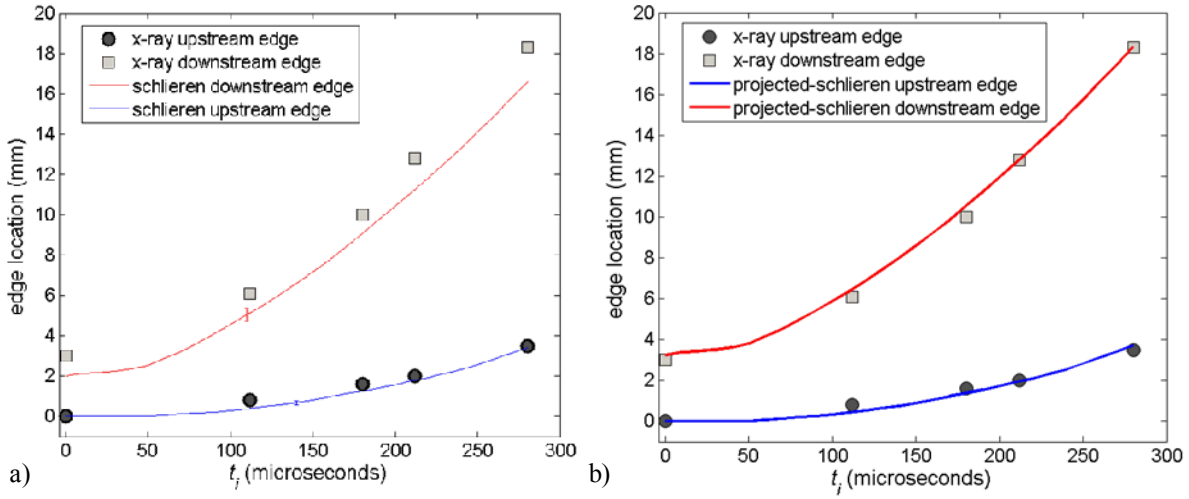

Fig. 16 A comparison of the upstream and downstream particle field edge positions during a Mach 1.66 interaction given from the x-ray measurements the schlieren imaging: a) actual schlieren edge position, and b) projected-schlieren edge position to account for geometric distortion

B. Geometric Distortion in the Current Data

An explanation for the discrepancy between the two measurement techniques can be given using the geometry in Fig. 17. The coordinate origin in the figure now corresponds to the x-ray point source location. Owing to the diverging rays of the point source, an intensity profile will appear broadened with the four images of the four corners of the particle field appearing at four different locations on the detector image plane. This is true even if the angle between the center of the particle field and the source centerline θ, in Fig. 6, is zero. (Although $\theta = 0$ would result in the minimum broadening, as is discussed in the next section.) As θ increases, the apparent broadening will increase further contributing to the geometric distortion. For the current work, the initial location of the downstream edge of the particle field was at about X_1 = -20 mm. With increasing time, the particle field propagated downstream therefore reducing geometric distortion.

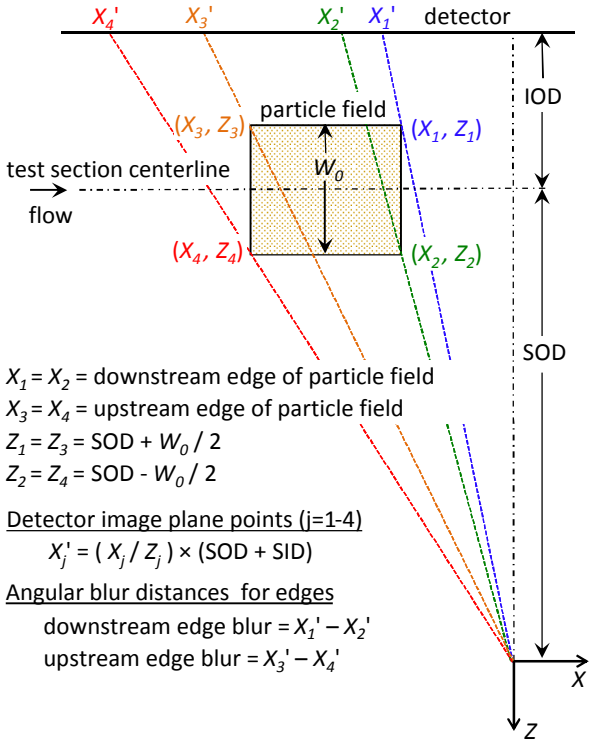

Fig. 17 Schematic illustrating the geometric distortion in the flash x-ray measurements. At t_i = 0, the downstream edge of the particle field was at about X_1 = -20 mm.

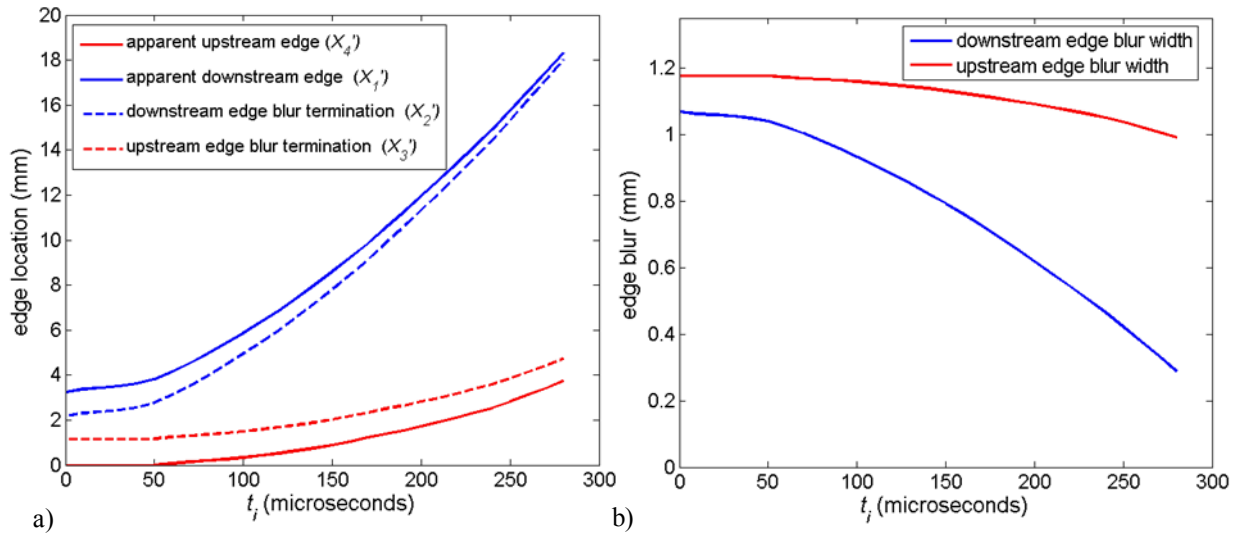

Fig. 18 Plots illustration blur of the particle field edges: a) position of particle field corner in the image plane, and b) edge blur widths defined as the distance between corner image locations.

The schlieren edge position data shown in Fig. 16a were projected onto the image plane in Fig. 17. A comparison between the projected-schlieren data and the x-ray data is shown in Fig. 16b. The good agreement for both edges suggests that the above explanation for geometric broadening is correct.

According to Fig. 17, the edges of the particle field will appear blurred with a false, geometrically induced gradient. The downstream edge will appear blurred over the distance X_1'- X_2' and the upstream edge blur distance will be X_3'- X_4'. Since the true streamwise variation of the particle field is not known *a priori*, the data cannot be corrected to remove the geometric distortion in these regions. However, it is necessary to understand the regions in which geometric distortion is prevalent to avoid making incorrect physical observations. The previous schlieren data

were used to generate the expected image locations for the particle field corners (X_1'through X_4'). These image locations are shown in Fig. 18a. Figure 18b shows the geometric blur widths for the downstream (X_1'- X_2') and upstream edges (X_3'- X_4'). These blur widths are used to define the blurred regions of the profiles in Fig. 11.

Finally, Fig. 19 compares the expected true width of the particle field to the broadened width (X_1'- X_4'). The figure indicates that the current x-ray profiles are broadened by about 1.3 mm.

C. Geometric Distortion for an Ideal Experimental Setup

To minimize geometric distortion, the ideal experimental configuration would have the streamwise center of the particle field coincident with the centerline of the detector. Such a setup is shown in Fig. 20.

Figure 21a shows the blur width for the setup based on the particle field edges given by the previous schlieren imaging. As the particle field spreads with time, the blur width of both the upstream and downstream edge increases at the same rate. Figure 21b compares the width measured with schlieren imaging to the broadened width expected for the ideal configuration. Even with the best possible x-ray imaging system configuration, the diverging rays of the point source result in a broadening of about 1.3 mm at an interaction time of 280 μs.

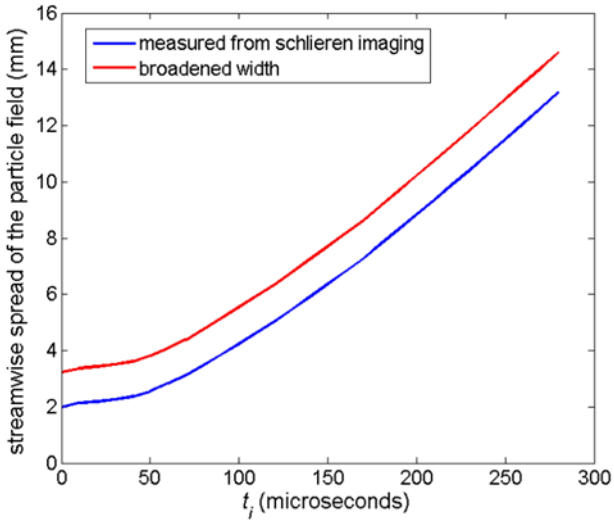

Fig. 19 Comparison of measured particle field width to that which would be given by the current x-ray experimental configuration (i.e, the broadened width).

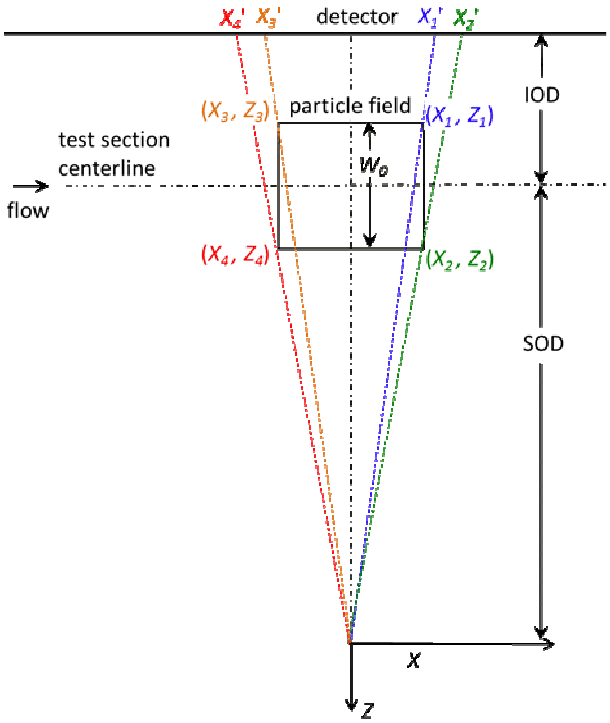

Fig. 20 Schematic illustrating the geometric distortion for the ideal flash x-ray experimental configuration.

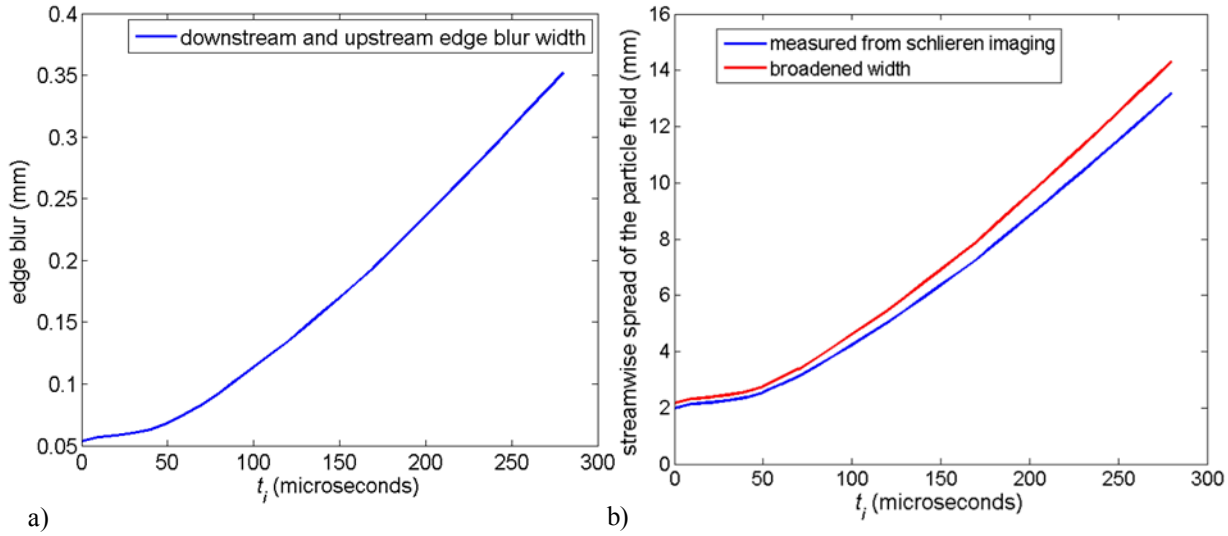

a) b)

Fig. 21 Plots showing the geometric distortion for the experimental configuration of Fig. 20: a) edge blur widths, and b) measured particle field width compared to the expected broadened width.

Acknowledgments

This work was supported by an internal Laboratory Directed Research and Development (LDRD) grant. The authors gratefully acknowledge this source of support.

References

[1]Zhang, F., Frost, D. L., Thibault, P. A., and Murray, S. B., "Explosive Dispersal of Solid Particles," *Shock Waves*, Vol. 10, 2001, pp. 431-443.

[2] Boiko V.M., Kiselev V.P., Kiselev S.P., Papyrin A.N., Poplavsky S.V., and Fomin V.M., "Shock wave interaction with a cloud of particles," *Shock Waves* Vol. 7, 1997, pp. 275-285.

[3]Rogue, X.,Rodriguez, G., Haas, J. F., and Saurel, R., "Experimental and numerical investigation of the shock-induced fluidization of a particles bed," *Shock Waves*, Vol. 8, 1998, pp. 29-45.

[4]Wagner, J. L., Beresh, S. J., Kearney, S. P., Trott, W. M., Castaneda, J. N., Cooper, Pruett, B.O., and Baer, M. R., "A Multiphase Shock Tube for Shock Wave Interaction with Dense Particle Fields," *Experiments in Fluids*, accepted for publication.

[5]Wagner, J. L., Beresh, S. J., Kearney, S. P., Trott, W. M., Castaneda, J. N., Cooper, Pruett, B.O., Cooper, M. A., and Baer, M. R., "Development of a Multiphase Shock Tube for Energetic Materials Characterization," AIAA Paper 2010-4535, June 2010.

[6]Wagner, J. L., Beresh, S. J., Kearney, S. P., Trott, W. M., Castaneda, J. N., Pruett, B. O., and Baer, M. R., "Interaction of a Planar Shock with a Dense Field of Particles in a Multiphase Shock Tube," AIAA Paper 2010-188, January 2011.

[7]Wagner, J. L., Beresh, S. J., Kearney, S. P., Trott, W. M., Castaneda, J. N., Pruett, B. O., and Baer, M. R., "Interaction of a Planar Shock with a Dense Field of Particles," International Symposium of Shock Waves Paper 2826, July 2011.

[8]Ramírez, A. I., Som, S., Aggarwal, S. K., Kastengren, El-Hannouny, E. M. , Longman, D. E., and Powell, C. F., "Quantitative X-ray measurements of high-pressure fuel sprays from a production heavy duty diesel injector," *Experiments in Fluids*, Vol. 47, 2009, pp. 119-134.

[9]Lee S. J., and Kim G. B., "X-Ray Particle Image Velocimetry for Measuring Quantitative Flow Information Inside Opaque Objects," *Journal of Applied Physics*, Vol. 94, No. 5, 2003, pp.3620-3623.

[10]Im, K.-S., Fezzaa, K., Wang, Y. J., Liu, X., Wang, J., and Lai, M.-C., "Particle tracking velocimetry using fast x-ray phase-contrast imaging," *Applied Physics Letters*, Vol. 90, 2007.

[11]Seeger A., Affeld K., Goubergrits L., Kertzscher U., and Wellnhofer E., "X-Ray-Based Assessment of the Three-Dimensional Velocity of the Liquid Phase in a Bubble Column," *Experiments in Fluids*, Vol. 31, 2001, pp. 193-201.

[12]Meekunnasombat, P., Oakley, J. G., Anderson, M. H., and Bonazza, R., "Experimental study of shock-accelerated liquid layers," *Shock Waves*, Vol. 15, 2006, pp. 383-397.

[13]Selman, J, *The Fundamentals of Imaging Physics and Radiobiology*, Charles C Thomas, 2000.

[14]Hubnell, J. H., Seltzer, S. M., "Tables of X-Ray Mass Attenuation Coefficients and Mass Energy-Absorption Coefficients from 1 keV to 20 MeV for Elements Z = 1 to 92 and 48 Additional Substances of Dosimetric Interest," *NIST X-ray Attenuation Databases* [online database], URL: http://www.nist.gov/pml/data/xraycoef/index.cfm.